Lab on a Chip

PAPER

View Article Online
View Journal | View Issue

Cite this: *Lab Chip*, 2025, **25**, 4660

Utility of an *in vitro* lymphatics on-chip model for rank ordering subcutaneous absorption of monoclonal antibodies†

Adriana Martinez Ledo, *[a] Gabriela Misiewicz,[a] Thomas Dimke,[b] William R. Tschantz,[c] Jillian Handel, ‡[d] Ryan Pelis,[a] Gerard Bruin,[b] Karoline Bechtold-Peters,[e] Manuel Sanchez-Felix,§[f] Sujal Deshmukh,[a] Seunggyu Kim,[g] Maria Proestaki[h] and Roger D. Kamm[gh]

The lymphatic vasculature plays a key role in the subcutaneous absorption of macromolecules (>16 kDa). Recent trends toward subcutaneous delivery of macromolecular therapeutics have brought awareness to the need for preclinical estimation of subcutaneous bioavailability prior to first-in-human studies. *In vitro* tools offer a low-cost means to inform molecule design and formulation and mitigate costly mistakes of under- or overestimation of therapeutic dose and exposure in clinical studies. Building on a previous engineered on-chip lymphatics platform, the utility of an *in vitro* model to rank therapeutic proteins based on lymphatic absorption was investigated. Lymphatics grown under a combination of interstitial flow and growth factor supplementation on-chip demonstrated *in vivo*-like morphology, phenotypic marker expression, and solute drainage rates after a 4-day culture period. Dextrans of increasing molecular weight were assessed on the model and demonstrated an inverse relationship between size and diffusion coefficient. Similarly, a reduced lymphatic transport on-chip was observed for large antibody aggregates compared to non-aggregated molecules. More importantly, lymphatic transport of a panel of nine therapeutic proteins and monoclonal antibodies successfully rank ordered these molecules based on their subcutaneous bioavailability in humans (Pearson r = 0.8929). The on-chip lymphatics model described here appears as a promising tool for rank ordering subcutaneous lymphatic absorption during early drug development to increase the potential for successful candidate selection moving toward the clinic.

Received 21st November 2024,
Accepted 10th July 2025

DOI: 10.1039/d4lc00988f

rsc.li/loc

1. Introduction

Therapeutic proteins (TPs) are an increasingly important therapy for chronic conditions, including immunologic and inflammatory diseases and cancer. They encompass various modalities, such as coagulation factors, recombinant cytokines, enzymes, growth factors, hormones, and monoclonal antibodies (mAbs) as notable examples.[1] TPs usually cannot cross cellular barriers and achieve their pharmacological effect by interacting with targets on the cell membrane surface or with soluble ligands in the tissue interstitial fluid or blood. Due to their large size, low cellular permeability and variable metabolic and/or degradation processes, TPs present limited oral bioavailability and need parenteral administration *via* intravenous (IV), intramuscular (IM), or subcutaneous (SC) injection.[1] The SC route is often favored over IV by patients and healthcare providers due to the ease of self-administration, the possibility of home administration, lower healthcare costs and time.[2–6]

After being injected under the skin dermis by a needle, TPs move through the SC tissue before reaching the local

[a] *Pharmacokinetic Sciences, Novartis Biomedical Research, Cambridge, MA 02139, USA. E-mail: adriana.martinez_ledo@novartis.com*
[b] *Pharmacokinetic Sciences, Novartis Biomedical Research, CH-4056 Basel, Switzerland*
[c] *Biologics Research Center, Novartis Biomedical Research, Cambridge, MA 02139, USA*
[d] *Intern at Novartis Biomedical Research, Summer of Science Program, USA*
[e] *Technical Research and Development, Novartis Pharma AG, 4002 Basel, Switzerland*
[f] *Novartis Biomedical Research, Cambridge, MA 02139, USA*
[g] *Department of Mechanical Engineering, Massachusetts Institute of Technology, Cambridge, MA 02139, USA*
[h] *Department of Biological Engineering, Massachusetts Institute of Technology, Cambridge, MA 02139, USA*
† Electronic supplementary information (ESI) available. See DOI: **https://doi.org/10.1039/d4lc00988f**
‡ Present address: Neptune Bio, 430 East 29th St, West Tower, Suite 1410, New York, NY 10016, USA.
§ Present address: Halozyme Therapeutics, Inc., 12390 El Camino Real, San Diego, CA 92130, USA.

blood or lymphatic capillaries prior to entering the systemic bloodstream. The SC tissue, or hypodermis, is in between the intradermal (ID) and the IM space and mainly consists of fat cells and connective tissue as well as nerves, blood, and lymphatic capillaries.[7] The mechanisms of fluid dispersion through the SC tissue microstructure are not well understood, in part due to experimental difficulties in observing dynamic device–drug–tissue interactions *in vivo* and *in situ* at a suitable resolution. From a pharmaceutical and biological point of view, injected TPs undergo hindered diffusion through the extracellular matrix (ECM) in the interstitial space and finally enter systemic circulation by crossing endothelial borders of blood and lymphatic vessels. Uptake of TPs after SC injection is largely driven by convective transport, with transcytosis *via* the neonatal Fc receptor (FcRn) having only a minor contribution for IgG molecules. In line with other TPs for which the percentage of recovery in lymphatic *versus* blood vessels is increasing with increasing molecular weight, mAb absorption after SC administration is nearly exclusively facilitated by the lymphatic system rather than the vascular system. The lymphatic system consists of a vast network of vessels throughout the body and acts as a one-way transport pathway that returns fluid, macromolecules, and immune cells from the interstitial space of tissues to the systemic circulation through the thoracic duct. Lymphatic vessels carry lymph, a fluid mostly composed of water that has escaped from the blood capillaries into the interstitial spaces, and work in parallel with the blood venous system to maintain tissue fluid homeostasis thereby avoiding edema.[8] Because the flow of lymph fluid in lymphatic vessels is very slow compared to the blood flow in capillary vessels, the resulting absorption process of mAbs into the systemic circulation after SC administration is also slow, with a corresponding slow increase in serum concentration and delayed time of the maximum concentration (T_{max}) with frequent values of T_{max} around 6–8 days. A model-based analysis suggests that lymphatic flow rate is the most influential factor of T_{max}.[9]

With multiple barriers to transport, TPs, especially mAbs, do not exhibit satisfactory absolute bioavailability after SC injection, *i.e.*, in some cases less than 50%. Uptake into the systemic circulation is impacted by numerous factors including drug molecular weight that affects lymphatic *versus* vascular capillary distribution, local capillary density, and interstitial pressure. Different injection locations (abdomen, thigh, arm) or tissue beds (ID, SC, IM) are also known to impact absorption kinetics, most likely due to localized tissue morphology differences. Strategies to improve absolute bioavailability after SC administration during drug development are limited by the lack of reliable preclinical testing models and a thorough understanding of the absorption processes. Animal models have been largely used to study the physiological function and transport mechanisms of lymphatics as well as their role in diseases such as inflammation and cancer progression.[10] Although animal studies can fully reproduce physiological responses, they offer little control over local environmental cues and make it hard to separate and describe direct and indirect systemic effects, and their results are often not easily translated to humans due to anatomical and physiological differences between species.[11] This has led to the development of microfluidic technologies that address these issues by growing human-derived cells in three-dimensional (3D) environments that resemble tissue structure with exact control of the cellular microenvironment.[12] Very few of these microfluidic technologies enable measurements of lymphatic transport.[8,13–15]

Building on previous technology[14] describing a microfluidic approach to generate functional lymphatic microvascular networks in a 3D hydrogel compartment, in this work we sought to increase the speed and throughput of this technology as well as to expand its application. We screened for the optimal balance of growth factors and interstitial fluid flow to induce sprouting of lymphatic endothelial cells and achieve *in vivo*-like lymphatic vessel morphology in a 4-day culture period. Subsequently, we quantified the tissue drainage functionality of our engineered lymphatic microvasculature by which we validated solute drainage rates comparable to *in vivo* measurements. Lymphatic on-chip transport of a panel of marketed mAbs and TPs as well as mAbs in development at Novartis was measured by a new plate-reader-based methodology. The *in vitro–in vivo* correlation (IVIVC) between lymphatic transport on-chip and absolute subcutaneous bioavailability in humans was explored and successfully rank-ordered the panel of molecules based on their potential for high subcutaneous absorption.

2. Materials and methods

2.1 Protein labeling and characterization

A panel of marketed IgG1 monoclonal antibodies (mAbs) as well as a fusion protein and IgG1 and IgG4 mAbs under development at Novartis were used in this study. Proteins were conjugated with Alexa Fluor 555 NHS Ester (Life Technologies, Carlsbad, CA, USA) after being dialyzed from the supplied formulation buffers into PBS (Cytiva SH30258.01). 10 mg of each protein was conjugated at concentrations between 5 and 10 mg mL^{-1} with 10 equivalents of the AF555 dye for 4 h at 4 °C. The samples were then buffer exchanged using PD10 desalting columns (Cytiva 17085101) into their original formulation buffers and analyzed for monomeric status and concentration by size-exclusion chromatography multi-angle light scattering (SEC-MALS).

SEC-MALS was carried out on an Agilent 1260 Bioinert system equipped with Wyatt Treos miniDAWN and Optilab refractive index detectors. Separation was performed using a S200INC 5/150GL size-exclusion column (Cytiva) and Dulbecco's PBS supplemented with 150 mM NaCl and 1 mM

EDTA as the mobile phase at a flow rate of 0.45 mL min^{-1}. UV wavelength was monitored at 280 nm to detect the protein signal in all samples, and the vis wavelength at 555 nm was also monitored for labeled proteins (Fig. S1 and S2†).

2.2 Lymphatic endothelial cell culture

Human dermal microvascular endothelial cells (LECs) (CC-2543, lot 21TL076034; Lonza, Basel, Switzerland) were cultured in VascuLife Endothelial Medium supplemented with VascuLife VEGF LifeFactors kit (Lifeline, Oceanside, CA, USA) at 37 °C and 5% CO_2 in a humidified incubator. For expansion, cells were seeded at 2500 viable cells per cm^2 and medium was refreshed every 2 days. Cells at passage 4–9 were used for seeding in microfluidic devices before reaching confluence.

2.3 Generation of lymphatic microvasculature on-chip

A microfluidic device from AIM Biotech (idenTx 3 Chip; AIM Biotech, Central Region, Singapore) was used to assemble the subcutaneous (SC) lymphatics on-chip. Each device consists of three channels: one central channel, where a fibrin extracellular matrix (ECM) was injected to model the SC interstitium, and two parallel medium channels on either side – one cell-free channel and one LEC channel (Fig. 1A). Prior to cell seeding on-chip, luer connectors were added into ports of the cell-free channel to enable the connection of syringes for hydrostatic pressure-driven flow generation across the central channel (Fig. S3†). Stock solutions of fibrinogen and thrombin from bovine plasma were prepared, sterile-filtered (0.22 μm) and distributed as ready-to-use aliquots for the generation of fibrin ECM in the central channel. Fibrinogen (F8630, Lot SLCJ9736; Sigma-Aldrich, St. Louis, MO, USA) was dissolved at 5 mg mL^{-1} (2.5 mg mL^{-1} ECMs) or 10 mg mL^{-1} (5 mg mL^{-1} ECMs) in PBS pH 7.4 without calcium and magnesium (Gibco, Life Technologies, Carlsbad, CA, USA) in a water bath for 1 h. Thrombin (T4648, Lot SLBW2056; Sigma-Aldrich) was dissolved at 100 U mL^{-1} in PBS supplemented with 0.1% (w/v) bovine serum albumin (A1653, Lot SLCH5923; Sigma-Aldrich).

For chip assembly, fibrinogen and thrombin stocks were thawed on ice and thrombin stock was diluted at 4 U mL^{-1} in VascuLife basal medium (Lifeline) without supplementation. Thrombin and fibrinogen were mixed in equal parts (v : v) on ice and 14 μL of the mixture were immediately injected into the chip central channel. After injection, the device was incubated at 37 °C for 15–20 min in an enclosed container with a moist environment, yielding an ECM gel of 2.5 mg mL^{-1} or 5 mg mL^{-1} fibrinogen and 2 U mL^{-1} thrombin concentration. Next, the lymphatic endothelial cell (LEC) channel was coated to promote cell attachment by injecting 40 μL of a 0.1 mg mL^{-1} solution of fibronectin (FC010-5; EMD Millipore, Burlington, MA) in PBS pH 7.4. The device was incubated at 37 °C for 45 min while a LEC suspension (4×10^6 cells per mL) was prepared in VascuLife supplemented with a LifeFactors kit plus an additional 8% (v/v) fetal bovine serum (FBS, Invitrogen, Carlsbad, CA, USA), resulting in a final FBS concentration of 10% (v/v). Soluble fibronectin was carefully rinsed out of the LEC channel with VascuLife 10% FBS immediately prior to cell seeding. LEC suspension (30 μL) was added to the channel and the device was tilted 90° for 15–20 min at room temperature to promote cell adhesion to the central ECM gel. Before placing into the incubator, the cell-free channel was filled with 30 μL of medium and the top and bottom capacitors of the LEC channel were filled with roughly 100 μL each to establish a slight pressure gradient promoting cell growth towards the ECM. The seeded device was incubated for 24 h at 37 °C and 5% CO_2 to allow the formation of a lymphatic tubule in the LEC channel.

To induce microvascular sprouting from the lymphatic tubule into the ECM, LECs were subjected to three stimuli: interstitial flow ("high" and "low"), growth factor (GF) supplementation, and a combination of both. For high flow generation, a hydrostatic pressure gradient between both medium channels was induced by inserting 3 mL (EXCELINT, Redondo Beach, CA, USA) and 1 mL (EXCELINT) pre-cut syringes into the luers of the medium channel and filling them with VascuLife 10% FBS until 1 and 0.65 mL, respectively, to yield a ~4.2 and 6.3 cm pressure head (Fig. S3†). Low flow was induced by filling the luer connectors with 0.2 mL of medium (~1.8 cm pressure head). VascuLife 10% FBS was supplemented with recombinant human vascular endothelial growth factor C (VEGF-C), angiopoietin 1 (ANG-1) and heparin growth factor (HGF) (Peprotech, Cranbury, NJ, USA) at 17 ng mL^{-1} each when both flow and growth factor supplementation were combined. A summary of the conditions tested is included in Table 1, where the condition selected for optimal LEC sprouting on-chip (condition 5, high flow + growth factors) is highlighted. The device was placed in an incubator with medium replacement every 24 h until it was ready for analysis, amounting to a 5-day workflow (Fig. 1B).

2.4 Immunofluorescence staining of lymphatic phenotypic markers

At the end of the 4-day culture period, chips were washed 2–3 times with blocking solution consisting of 10% (v/v) goat serum (Gibco) in PBS pH 7.4. Chips were then fixed for at least 40 min in the dark at room temperature (RT) with a 4% paraformaldehyde (Electron Microscopy Sciences, Hatfield, PA, USA) solution in PBS pH 7.4 (Gibco) added to the luers of the medium channel (100 μL) and the capacitors of the lymphatic endothelial cell (LEC) channel (30 μL). After fixation, chips were blocked with blocking solution (100 and 30 μL for medium and LEC channel, respectively) for 1 h, then incubated overnight at 4 °C with 50 μL of primary antibodies against human vascular endothelial cadherin (VE-cadherin) (ab33168 Abcam, Cambridge, UK) and human endothelial hyaluronan receptor 1 (LYVE1) (ab10278 Abcam) diluted 1 : 50 in blocking solution. After incubation, chips were washed 4 times for 15 min each with 0.1% (w/v) bovine serum albumin (126593; EMD Millipore, Burlington, VT, USA)

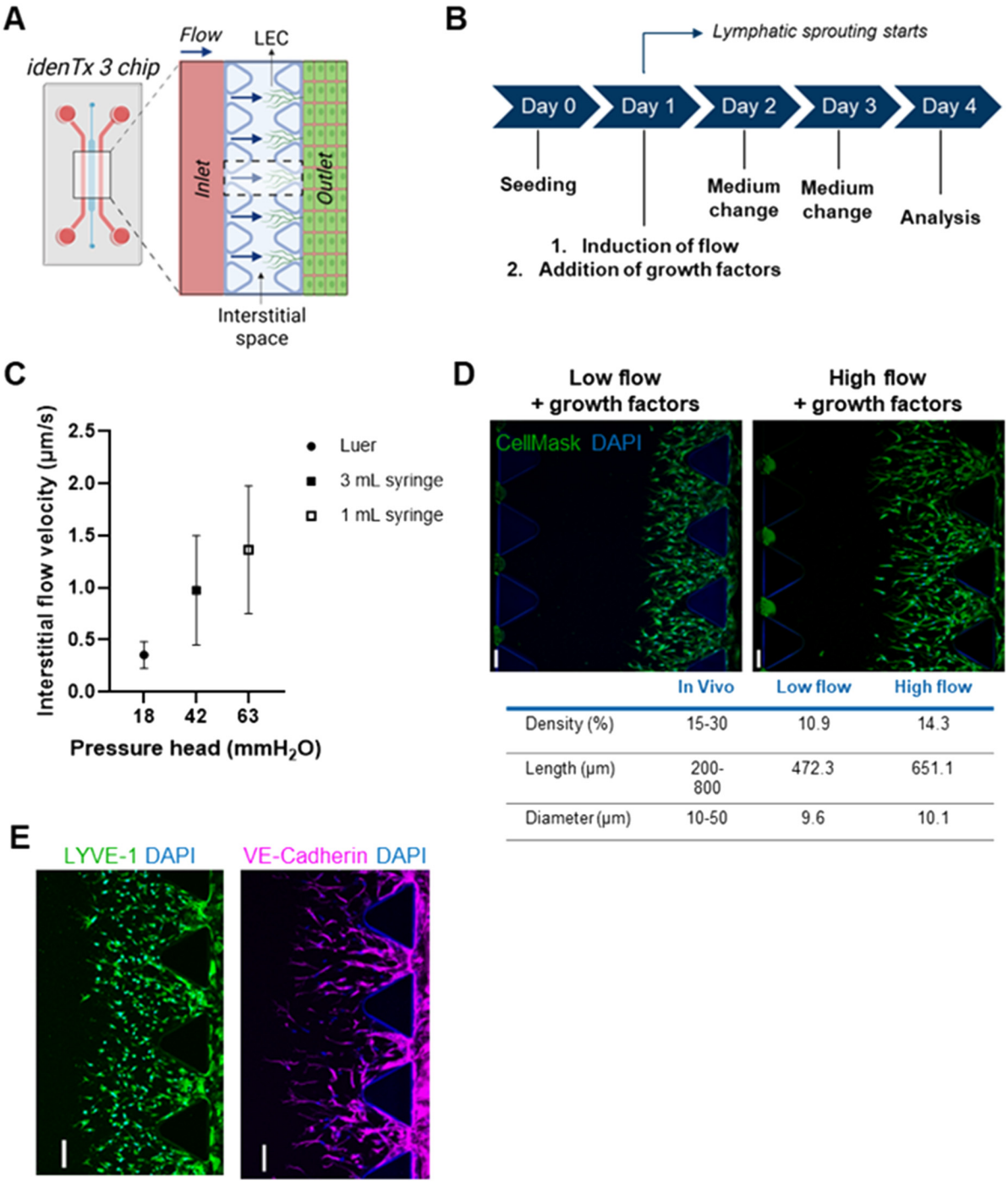

	In Vivo	Low flow	High flow
Density (%)	15-30	10.9	14.3
Length (μm)	200-800	472.3	651.1
Diameter (μm)	10-50	9.6	10.1

Fig. 1 Optimization and characterization of the subcutaneous (SC) lymphatics on-chip model. (A) Schematic depicting the 3-channel idenTx 3 microfluidic chip used to assemble the SC lymphatics on-chip. Lymphatic endothelial cells (LECs) are seeded on the right channel (outlet) and generate lymphatic capillaries into the fibrin matrix in the central channel (interstitial space). Created in BioRender. Martinez Ledo, A. (2025), **https://BioRender.com/w48q949**. (B) Schematic showing the timeline of the experimental workflow from chip seeding to analysis. (C) FRAP was performed with 150 kDa FITC-dextran to measure interstitial flow velocities in the fibrin matrix upon induction of hydrostatic pressures driven by luer connectors (low flow, 18 mm H_2O) or luer connectors coupled with syringes (high flow, 42 or 63 mm H_2O). Data shown as mean ± SD of at least six chips. (D) Maximum intensity projections of CellMask staining of cell membranes (green) used to quantify length and density of lymphatic capillaries grown under low or high flow in the presence of growth factor supplementation. Cell nuclei are stained with DAPI (blue). Scale bar = 100 μm. (E) Maximum intensity projections of immunofluorescence staining detecting LYVE-1 (left, green) and VE-cadherin (right, purple) in the lymphatic capillaries within the extracellular matrix (ECM). Cell nuclei are stained with DAPI (blue). Scale bar = 100 μm.

and 0.04% Tween 20 (VWR, Radnor PA, USA) in PBS pH 7.4 and then incubated overnight at RT with 50 μL of secondary antibody, Alexa Fluor 647 (A-21245; Invitrogen, Waltham, MA, USA) diluted 1 : 200 in wash buffer. The following day, chips

Table 1 Conditions used to optimize lymphatic capillary growth on-chip indicating chip set up, established pressure head, growth factor supplementation and fibrinogen concentration

Condition	Chip set up	Volume (mL)	Pressure head (cm)	Flow ($\mu m\ s^{-1}$)	Growth factors	Fibrinogen ($mg\ mL^{-1}$)
1 (low flow + growth factors)	Luer	0.20	~1.8	0.35 ± 0.13	VEGF-C, ANG-1, HGF	2.5
2 (high flow)	Pre-cut 3 mL syringe	1	~4.2	0.97 ± 0.52	—	2.5
3 (high flow)	Pre-cut 1 mL syringe	0.65	~6.3	1.36 ± 0.61	—	2.5
4 (high flow + growth factors)	Pre-cut 3 mL syringe	1	~4.2	0.97 ± 0.52	VEGF-C, ANG-1, HGF	2.5
5 (high flow + growth factors)[a]	Pre-cut 1 mL syringe	0.65	~6.3	1.36 ± 0.61	VEGF-C, ANG-1, HGF	2.5
6 (high flow + growth factors in 5 $mg\ mL^{-1}$ fibrin ECM)	Pre-cut 1 mL syringe	0.65	~6.3	1.36 ± 0.61	VEGF-C, ANG-1, HGF	5

[a] Condition selected for optimal LEC sprouting and ECM coverage as described in section 3.1.

were washed with PBS as described above, stained for 5 min with 50 μL of 4′,6-diamidino-2-phenylindole (DAPI, Sigma) diluted at 2.5 $\mu g\ mL^{-1}$ in PBS pH 7.4, washed again and stored at 4 °C protected from light until imaging. Chips were imaged using an Airy Scan LSM 880 inverted confocal microscope equipped with a Zeiss Plan-Apochromat 10×/0.45 M27 objective. Images shown are maximum projections of Z-stacks acquired every 1.84 μm using 405 nm and 633 nm lasers.

2.5 Analysis of lymphatic capillary morphology

The morphology of lymphatic capillaries generated under high flow and low flow in the presence of growth factors was analyzed using a distribution of ImageJ, FIJI1.5n.[16] Chips were fixed as described in section 2.4 and stained with 50 μL of CellMask™ orange plasma membrane stain (C10045, Invitrogen) diluted 1 : 100 in PBS pH 7.4 (Gibco) overnight at 4 °C. Chips were then washed twice with PBS pH 7.4, stained for 5 min with 50 μL of 4′,6-diamidino-2-phenylindole (DAPI, Sigma) diluted at 2.5 $\mu g\ mL^{-1}$ in PBS pH 7.4 and washed again before imaging. A region in the middle of the central matrix channel was selected and imaged throughout the full thickness of the device (~40 μm Z-stack) using an Airy Scan LSM 880 inverted confocal microscope equipped with a Zeiss Plan-Apochromat 10×/0.45 M27 objective. Images shown are maximum projections of Z-stacks acquired every 1.09 μm with 405 and 561 nm lasers.

Before analysis, a region of interest (ROI) in the middle of the central extracellular matrix (ECM) channel was selected from the maximum Z-stack projections to measure lymphatic vessel density, thickness, and length. The selected ROI had a length of 1500 μm and captured the full width of the ECM from inlet to outlet channels including the triangular posts in the device (Fig. 1A, dotted rectangle). ROI images were then inverted and adjusted for brightness and contrast before applying the vessel analysis plug-in[17] to quantify vessel density and thickness. Vessel length was measured from the edge of the outlet medium channel (lymphatic tubule) to the tip of the vessel using the straight selection feature. Five measurements were performed per ROI and an average length in microns was reported.

2.6 Interstitial flow measurements

A modification of the fluorescence recovery after photobleaching (FRAP) technique previously described by Serrano *et al.*[14] was used to quantify the interstitial flow velocities generated by hydrostatic pressure differences established across the extracellular matrix (ECM). Lymphatic endothelial cells (LECs) were grown in the chips under the optimized culture conditions described in section 2.1, and chips were analyzed at day 4. FRAP was performed with 150 kDa fluorescein isothiocyanate (FITC) dextran and both syringe- and luer-driven pressure head differences to measure the interstitial velocities based on the convection of a photobleached spot achieved during LEC chip culturing and molecule transport measurements, respectively. For the syringe setup, the cell culture medium in the syringes and corresponding channel was removed and syringes were filled to either the 1 mL mark (~4.2 cm, 3 mL syringes) or the 0.65 mL mark (~6.3 cm, 1 mL syringe) (Fig. S3†) with FITC-dextran 150 kDa (Sigma-Aldrich, Burlington, MA, USA) diluted to 10 $\mu g\ mL^{-1}$ in VascuLife medium (Lifeline) supplemented with 10% fetal bovine serum (FBS, Gibco). For the luer setup, medium in the luers and corresponding channel was removed and replaced by 0.2 mL of 150 kDa FITC-dextran solution (~1.8 cm, Fig. S3†). Chips were subsequently incubated for 5 h prior to analysis to allow the tracer to equilibrate and distribute homogeneously across the ECM. FRAP measurements were performed in an Airy Scan LSM 880 inverted confocal microscope equipped with a Plan-Achromat 20×/0.8 M27 Zeiss objective using a 488 nm laser. At least 4 regions of interest (ROIs) of 38 μm diameter were selected from top to bottom of the ECM. ROIs were photobleached using zoom bleach and images were captured immediately every 0.64 s during 10–30 cycles under atmosphere-controlled conditions (37 °C, 5% CO_2). The time-lapse image series were analyzed by MATLAB (MathWorks, version R2017b) frap-analysis plugin[18] to calculate the flow velocities at each pressure head difference. The slope of the linear regression of interstitial flow velocity *versus* pressure head was used to calculate a combined hydraulic permeability (K) of the gel matrix and

lymph capillary membrane (Fig. S4†). Interstitial flow velocities were measured by FRAP with 4 and 500 kDa FITC-dextran (Sigma-Aldrich) for the luer setup following the same protocol. Diffusion coefficients of all FITC-dextrans were extracted by the same MATLAB plugin after FRAP measurements were performed with the luer setup and used for computational fluid dynamics (CFD) simulations (Fig. S5†).

2.7 Generation and characterization of IgG aggregates

A commercially available goat anti-mouse IgG labeled with DyLight® 650 (Abcam ab96882) was used to assess the impact of antibody aggregation on lymphatic transport on-chip. Two previously described methods were used to induce IgG aggregation: shear and heat stress.[19–21] For shear stress, the commercial IgG stock was diluted to 100 μg mL^{-1} in PBS pH 7.4 (Gibco) with 0.2% (w/v) bovine serum albumin (EMD Millipore) and 0.25 mL were added to 5 mL glass vials in triplicate. Vials were stirred with a magnet (0.625 mm × 10 mm) at 300 rpm and room temperature for 24 h. For heat stress, IgG was diluted as described previously, and 0.25 mL were added to 1.5 mL low binding tubes (Eppendorf, Hamburg, DE). Tubes were incubated at 74 °C for 12 min on an Eppendorf Thermomixer R protected from light. Stressed samples were kept at 4 °C for up to a week before use. The resulting IgG aggregates were analyzed by sodium dodecyl sulfate polyacrylamide electrophoresis (SDS-PAGE) to estimate aggregation compared to unstressed IgG.

SDS-PAGE was performed in 4–20% linear gradient Tris–glycine gels (Mini-PROTEAN® TGX™, Invitrogen) under native conditions. Samples were diluted with water and mixed with Bio-Rad native buffer before loading into the gels (200 ng of protein per lane). Gels were run in a XCell SureLock mini-cell electrophoresis system at 200 V for 1 h at room temperature. Unstressed IgG samples were diluted to 100 μg mL^{-1} in PBS pH 7.4 with 0.2% (w/v) BSA prior to analysis to match the stressed samples matrix. Protein bands were detected by LabSafe GEL Blue (G-Biosciences, St. Louis, MO, USA) and gels were scanned with a Bio-Rad densitometer and software. The Precision Plus Protein Dual Xtra Prestained Protein Standards 2–250 kD (Bio-Rad) was used as a molecular size reference.

2.8 Lymphatic solute drainage rate and percentage transport

Solute drainage rate and percentage lymphatic transport of test molecules were measured by confocal microscopy and UV spectroscopy, respectively, on day 4 post-seeding following LEC growth condition 5 described in Table 1. Fluorescent test molecules were diluted in VascuLife cell culture medium supplemented with 10% fetal bovine serum (FBS) to a concentration of 10 μg mL^{-1}, and 200 μL were distributed between the two luer connectors in the medium channel (inlet) to establish a hydraulic pressure difference resulting in an interstitial flow of ~0.35 μm s^{-1} through the fibrin extracellular matrix (ECM) (Fig. S3†). Over time, test molecules move through the ECM into the lymphatics by convection and diffusion, and lymphatic transport is measured by analyzing fluorescence intensity (surrogate for molecule concentration) in the downstream LEC channel (outlet) (Fig. 2A and B).

Solute drainage rate was calculated by measuring fluorescence intensity in the outlet channel over time using an Airy Scan LSM 880 inverted confocal microscope following the methodology described by Serrano *et al.*[14] Briefly, a series of 4 regions of interest (ROIs) selected from top to bottom of the outlet channel were imaged throughout the full thickness of the device (~40 μm Z-stack) every 2 min for up to a maximum of 60 min under atmosphere-controlled conditions (37 °C, 5% CO_2). Images were acquired with a Zeiss Plan-Apochromat 10×/0.45 M27 objective using a 488 nm (FITC-dextrans) or 633 nm laser (IgG DyLight® 650). At the end of the acquisition, a ROI of the same dimensions was applied to measure the fluorescence intensity in the source medium channel (inlet). FIJI1.5n[16] image analysis software was used to quantify the maximum fluorescence intensity of each ROI over time and calculate solute drainage rate with eqn (1):

$$\text{Solute drainage rate } (\text{min}^{-1}) = \frac{\Delta I_{\text{outlet}}}{\Delta t} \times \frac{1}{I_{\text{inlet}}} \quad (1)$$

where ΔI_{outlet} is the change in maximum fluorescence intensity within the outlet channel (lymphatic tubule) over the time of data acquisition (Δt), and I_{inlet} is the maximum fluorescence intensity of the source channel.

Percentage lymphatic transport was calculated by sampling the outlet channel at defined single time points, measuring fluorescence intensity by UV spectroscopy and extrapolating sample concentrations using calibration curves (0–10 μg mL^{-1}) prepared in VascuLife supplemented with 10% fetal bovine serum (FBS). At each time point (30 min, 1 h, 2 h or 4 h), the total volume in the outlet channel was collected (~8–10 μL) and the experiment terminated. Subsequently, 5 μL of the collected sample were added to a black bottom 384 plate (Greiner Bio-One, Kremsmünster, AT, EU) with 45 μL of VascuLife (+10% FBS) before measuring the fluorescence intensity in a Synergy H4 Hybrid reader (BioTek, Winooski, VT, USA). Excitation/emission wavelengths were 620/680 nm and 550/580 nm for IgG Dylight650 and for the panel of test molecules, respectively. The fluorescence intensity of the source solutions added to the inlet was measured in the same way to calculate percentage lymphatic transport based on eqn (2):

$$\text{Lymphatic transport } (\%) = \frac{C_{\text{outlet}}}{C_{\text{inlet}}} \times 100 \quad (2)$$

where C_{outlet} is the concentration of the test molecule in the outlet at the defined time point and C_{inlet} is the

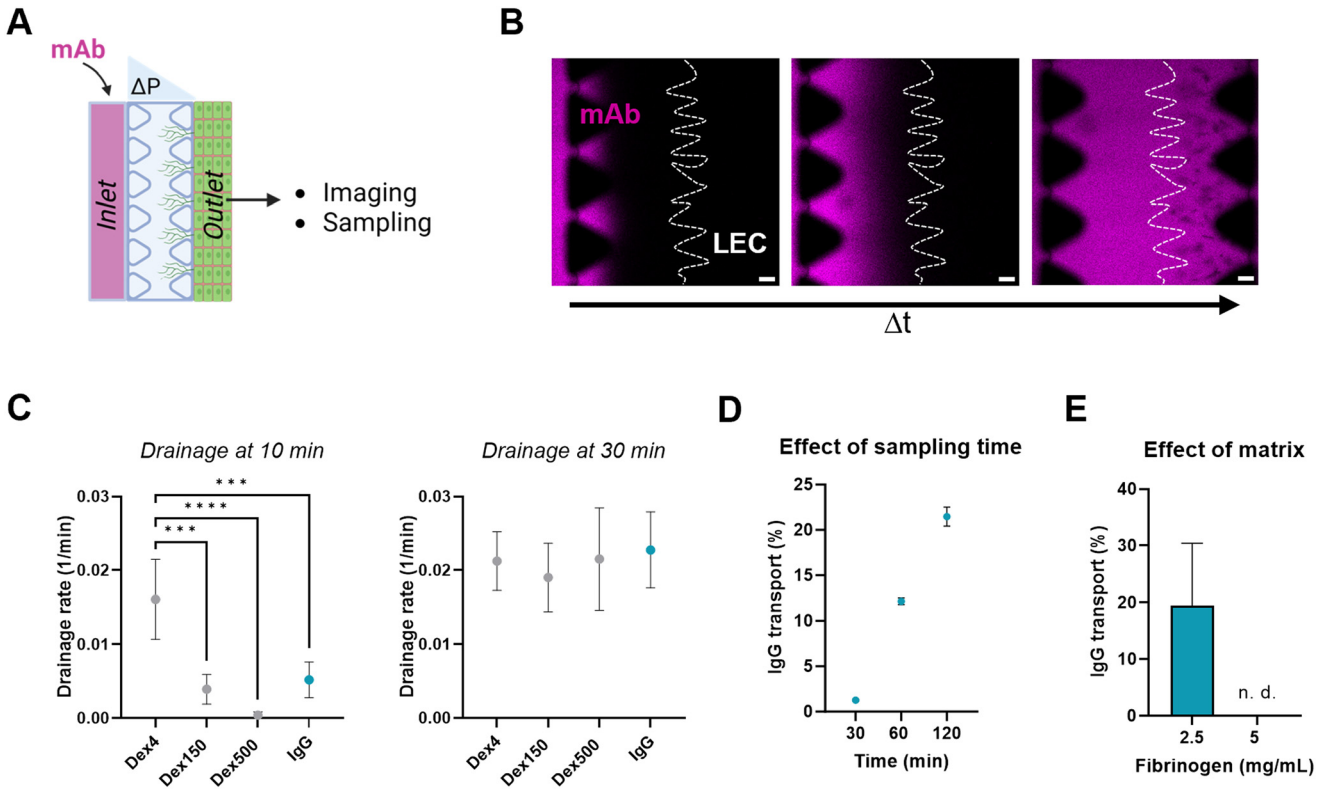

Fig. 2 Optimization and validation of lymphatic absorption on-chip. (A) Schematic of the lymphatic transport assay performed in the lymphatics on-chip. Monoclonal antibodies (mAbs) are introduced in the left channel (inlet), allowed to move through the fibrin matrix by convective and diffusive transport, and measured in the right channel (outlet). Created in BioRender. Martinez Ledo, A. (2025), **https://BioRender.com/o63o724**. (B) Confocal microscopy Z-slice showing the diffusive and convective transport of a model IgG-Dylight650 (purple) through the fibrin matrix toward the lymphatic capillaries (delineated by the dashed line) over time. Scale bar = 100 μm. (C) Drainage rate values obtained from the drainage rate *versus* time curves of fluorescein isothiocyanate (FITC)-dextrans of 4, 150 and 500 kDa compared to IgG-Dylight650 (150 kDa), run in each experiment as control, at 10 (left) and 30 min (right) time points. Data are mean ± SD (n = 3/4 FITC-dextrans; n = 8 IgG). A one-way ANOVA with Tukey's multiple comparisons test was performed to compare drainage rates at 10 min (***$P \leq 0.001$; ****$P \leq 0.0001$). (D) Percentage IgG-Dylight650 transported into the lymphatics at different time points as assessed by plate reader sampling of the outlet channel. Data represent mean ± SD (n = 3). (E) Percentage IgG-Dylight650 transported to the outlet channel at 2 h on lymphatic chips assembled with 2.5 and 5 mg mL^{-1} fibrin matrices. n.d. denotes not detected. Data represent mean ± SD (n = 3).

concentration of the test molecule added to the inlet channel.

2.9 Computational fluid dynamics model

A computational fluid dynamics (CFD) model was used to assess the effect of gel matrix and lymphatic barriers on the hydrostatic pressure driven flow and the transport of differently sized dextran molecules through the MPS to optimize sampling frequency and to explore the effect of sampling methods on the concentration–time profile. The simulations account for diffusion and convection processes in the three-dimensional space of the inlet and outlet channel as well as the gel matrix. They did not account for molecule–molecule and/or molecule–matrix interactions. Simulations were carried out in the commercial CFD software Simcenter STAR-CCM+ release 16.04.[22]

Due to the low fluid velocities within the three chip compartments (Reynolds number ≪1) (Fig. S6 and S7†), laminar flow with neglectable advective inertial forces (*i.e.* "creeping flow") was assumed.[23] Therefore, the Navier–Stokes equation was simplified to a linear relationship between velocity and spatial pressure gradient as defined in eqn (3):

$$\nabla p = -P_v \times v \quad (3)$$

where P_v is the isotropic porous viscous resistance[22] in the porous gel matrix.

Newtonian fluid with molecule size-dependent diffusion coefficients, a constant density and the dynamic viscosity of water at 37 °C was assumed. The segregated solver with a timestep size of 0.1 s was used during the flow field initialization (200 timesteps) and 1.0 s during the transient transport simulation.

According to the experimental setup with approximately 18 mm fill height (Fig. S3D†), the pressure difference between inlet and outlet channels was set to 147 Pa, and the initial mass concentration in the inlet channel and the concentration at the inlet boundaries were set to $C_{initial} = C_{inlet} = 0.01$ mg ml^{-1}. Dextran concentration was

monitored in the inlet and outlet channels at the center of the chip (representative for the confocal microscopy measurements) as well as over the whole fluid region of the outlet channel (representative for plate reader sampling). The fluid velocity in the gel matrix was reported only from the first half of the matrix, where no lymphatic absorption was applied. To achieve a specific surface area of 0.003 1 μm^{-1} as reported for lymphatic capillaries in MPS systems by Offeddu *et al.*,[24] a total of 5250 equally distributed locations were selected in the second half of the gel region. Similar to Soltani and Chen (2012),[25] these locations are used to withdraw fluid mass (by so-called sink terms) and account for the lymphatic absorption based on eqn (4):

$$\frac{dm_L}{dt} = \frac{AK_L}{\Delta x} \times \frac{\rho}{\mu} \times \Delta p_L \quad (4)$$

where Δp_L is the pressure gradient determined between the individual location in the gel and the corresponding location in the outlet channel. Δx, A and K_L are the thickness and surface area of the lymphatic capillary and its hydraulic conductivity, respectively. Due to the relatively large spaces in the lymphatic endothelial membrane assumed for paracellular transport into the lymph, for the meantime no further passages (*e.g.* transcellular transport) or barriers (*e.g.* reduced diffusion in the pore region) have been integrated into the model.

With the membrane properties in Table S1,† each absorption location can be seen as representative of the fluid uptake by a 25 μm diameter capillary with a surface area of A = 0.002 mm^2. The resulting matrix flow velocities in the gel are within the physiological range of 0.4 μm s^{-1} (target flow) and in line with the average interstitial flow of 0.35 μm s^{-1} measured for 150 kDa dextran (Fig. S5†). To ensure mass continuity and correct flow velocities in the outlet channel, the absorbed fluid mass is re-administered by a source term into the outlet channel close to the gel/channel interface (impermeable baffle), where it is available to the previously described concentration monitors. Averaged diffusion coefficients from fluorescence recovery after photobleaching (FRAP) measurements (methods section 2.6 and Fig. S5†) were used in the simulations for 4 and 150 kDa FITC-dextran at the target flow rate. For the 4 kDa FITC-dextran the molecule transport was additionally simulated with an increased flow rate of 0.6 μm s^{-1} (experimental flow), for which the model was adjusted by a 2-fold decrease in gel resistance and 2-fold increase in membrane conductivity (Table S1†). The same gel resistances and membrane conductivities were also applied in the variability investigation, in which variation in the pressure difference between inlet and outlet allowed to reproduce the experimentally observed range of flow rates (Fig. S5†) and the corresponding concentrations reached in the outlet channel after 0.5, 1 and 2 h (Fig. 3D).

2.10 Statistical analysis

Statistical analysis was performed using GraphPad Prism version 9.2.0 (San Diego, CA, USA). Where applicable, data are reported as the mean ± standard deviation (SD). Data were compared using either one-way or two-way ANOVA, and p-values ≤ 0.05 were considered statistically significant.

The correlation between *in vitro* antibody/therapeutic protein transport data and human subcutaneous bioavailability was investigated by linear regression and assessed using the R^2 and Pearson correlation coefficients. The *in vitro* transport data used for IVIVC analysis is the mean of data from four individual experiments (n = 3 chips per experiment) conducted on different days using different tissue culture preparations. A frequency distribution analysis was performed (bin width = 10; center of first bin = 5; center of last bin = 35) to guide the establishment of cut-off values to categorize the data in Fig. 5B into high (above 25%) and low (below 15%) transport (Fig. S8†).

3. Results

3.1 Lymphatic capillary growth and workflow optimization

Given the role of lymphatic capillaries in the subcutaneous (SC) absorption of macromolecules, this study evaluated the utility of an *in vitro* lymphatics on-chip model for rank ordering SC absorption of monoclonal antibodies (mAbs) toward predicting SC bioavailability in humans. The *in vitro* model builds upon previous technology described by Serrano *et al.*[14] and utilizes commercially available idenTx 3 chips from AIM Biotech to generate a lymphatic microvasculature within a fibrin extracellular matrix (ECM) mimicking the SC interstitium (Fig. 1A).

Culture conditions described by Serrano *et al.* were slightly modified to reduce the time required for lymphatic microvasculature sprouting, so that the model was ready for analysis within four days after seeding (Fig. 1B and section 2.3). Three parameters were modulated in order to maximize lymphatic sprouting in this time frame while recapitulating *in vivo*-like conditions:

(1) the flow of cell culture medium delivered to the lymphatic endothelial cells (LECs) through the fibrin ECM,

(2) the concentration of growth factors in the medium,

(3) the mechanical properties of the fibrin ECM.

The use of three different syringe luer-sip chip setups enabled the variation of interstitial flow velocities from "high", ~1 μm s^{-1} (1 and 3 mL syringes connected to luer), to "low", ~0.35 μm s^{-1} (luer connector alone) (Fig. 1C and S3†), while remaining within the reported physiological range for the SC interstitium.[26] The mechanical properties of the fibrin ECM were modified by adjusting the fibrinogen concentration from 2.5 mg mL^{-1}, previously reported by Serrano *et al.*,[14] to 5 mg mL^{-1}. The impact of the three parameters on lymphatic sprouting was first assessed by optical microscopy followed by a more detailed morphological analysis based on microvasculature staining and confocal microscopy imaging. Optical microscopy

imaging of 2.5 mg mL^{-1} fibrin ECMs showed that the induction of high flow without growth factor supplementation resulted in lymphatic capillaries of similar length but relatively sparse compared to those grown in the presence of growth factors under low flow (Fig. S9†). The combination of growth factors and high flow resulted in the longest and most dense lymphatic capillaries at the end of the 4-day capillary induction culture period (Fig. S9† and 1D). In agreement with previous reports,[27–29] LEC capillary formation on-chip was highly responsive to matrix mechanical properties. An increase of fibrinogen concentration from 2.5 to 5 mg mL^{-1} impaired lymphatic capillary sprouting even in the most optimal culture conditions (growth factors combined with high flow), resulting in the shortest capillaries among all the tested conditions during the same culture period (Fig. S9†).

Quantitative morphological analysis of lymphatic capillaries grown within 2.5 mg mL^{-1} fibrin ECMs in the presence of growth factors revealed that the use of high flow resulted in lymphatic vessel diameters (as small as ~10 μm) and ECM area coverages (~15%) very close to values observed in cryogenic sections *in vivo*[30–32] (Fig. 1D). The engineered lymphatics on-chip expressed the phenotypic markers lymphatic vessel endothelial hyaluronan receptor 1 (LYVE1) and vascular endothelial (VE) cadherin, further illustrating the physiological relevance of the *in vitro* model (Fig. 1E). mRNA levels of Forkhead Box C2 (FOXC2), a transcription factor expressed in lymphatic collecting vessels in response to flow,[33,34] decreased by ~40% in LECs cultured on-chip compared to LECs cultured on flask, supporting the induction of a lymphatic capillary phenotype in the lymphatics on-chip model (Fig. S10, ESI† Methods). Based on these morphological and phenotypical results, the condition of high flow in the presence of growth factor supplementation (Table 1, condition 5) was selected to grow the lymphatics on-chip for further downstream analysis.

3.2 Lymphatic transport method optimization

After establishing optimal growth conditions for the lymphatics on-chip, the model was applied to study the transport of a panel of reference macromolecules into the lymphatics: fluorescein isothiocyanate (FITC)-dextrans of varying molecular weight (MW) and an IgG labeled with DyLight650. Following the work of Serrano *et al.*,[14] test molecules were added to the inlet channel, permeated through the fibrin matrix by diffusion and convection and entered the lymphatic capillaries toward the outlet channel, where fluorescence intensity was continually measured by confocal microscopy to calculate drainage rate (Fig. 2A and B). For all molecules measured, the maximum drainage rate was approximately 0.025 min^{-1}, while the time to reach maximum drainage showed a negative correlation with MW: the 4 kDa and 500 kDa FITC-dextrans reached maximum values faster and slower than the IgG (150 kDa), respectively, while the 150 kDa dextran showed nearly identical drainage profiles (Tables S2–S5†). Consequently, if analyzing drainage at a single time point, molecules could be differentiated based on MW when measured at 10 min, but this resolution was lost when data were collected at 30 min (Fig. 2C). In line with previous literature,[14] differences in drainage values observed at 10 min correlated with the MW of the molecules: 4 kDa dextran > IgG ≈ 150 kDa dextran > 500 kDa dextran (Fig. 2C).

To improve the throughput of the confocal-based assay described by Serrano *et al.*,[14] we next evaluated the use of single time point sampling of the outlet channel combined with fluorescence plate reader analysis to assess lymphatic transport on-chip. With this methodology, lymphatic absorption is reported as the percentage of molecules transported from the inlet into the outlet channel at a single time point. Given that each chip can be sampled only once due to the small volume in the outlet channel, we selected only three time points (30, 60 and 120 min) to build a % transport-time profile similar to the drainage rate profiles obtained with confocal microscopy. Percentage IgG transport increased with time (Fig. 2D) and decreased with increased fibrinogen concentration, as expected due to the high MW of IgG molecules and the lower porosity of denser fibrin hydrogels[35,36] (Fig. 2E). Compared to confocal measurements, where drainage of IgG reached maximum values at 30 min (Fig. 2C), % IgG transported into the outlet channel was just above the detection limit of the plate reader after 30 min, while the fluorescence signal intensity was high at 120 min (Fig. 2D). Based on this, a 120 min time point was selected for lymphatic transport measurements to increase the dynamic range of the assay and better enable molecule differentiation. Parallel computational fluid dynamics (CFD) simulations were used to explain the time-lag differences in concentration–time profiles measured by confocal microscopy and fluorescence plate reader and to help optimize the plate reader sampling strategy (Fig. 3).

Confocal microscopy allows for a local sampling immediately next to the extracellular matrix (ECM)/outlet interface, reflecting the maximum molecule concentration measured over time in a small region in the center of the chip (Fig. 3A and B). Conversely, the whole fluid in the outlet channel is sampled for plate reader measurements, and the averaged concentrations of the total volume in the outlet channel are shown in scatter plots (Fig. 3C and D).

In order to compare with the CFD simulations, maximum molecule concentrations measured by confocal microscopy were normalized by reference values determined at the end of the measurements in the inlet channel. For 150 kDa FITC-dextran, confocal experimental data (grey squares) are in good alignment with the simulations (green dashed line), where concentration values reach ~0.005 mg mL^{-1} at 30 min (Fig. 3B). For 4 kDa FITC-dextran, those experimental data (grey circles) are in better alignment with the simulation performed under experimental flow (blue dashed line) compared to those from target flow conditions (blue dotted line). The discrepancy between experimental and

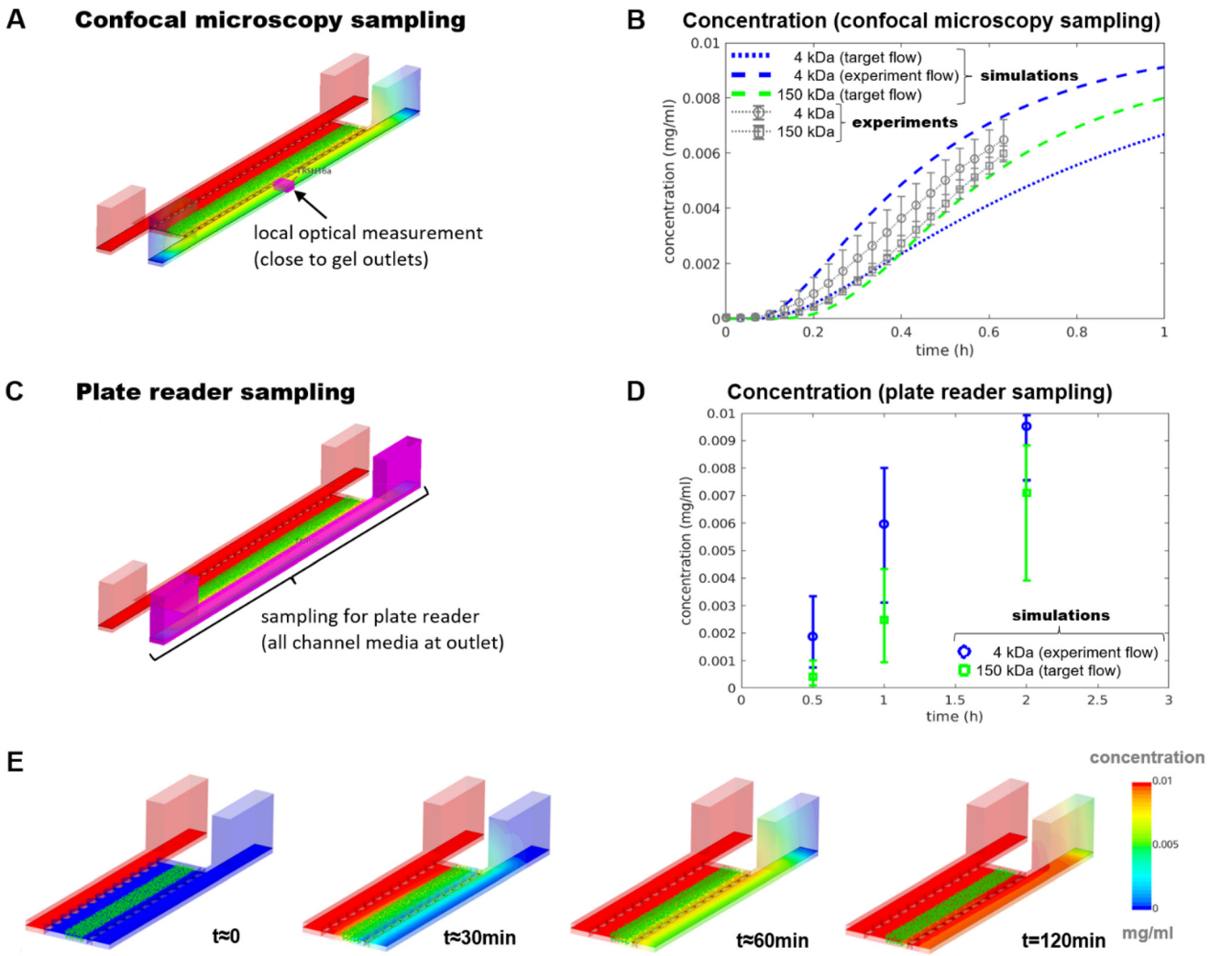

Fig. 3 Computational fluid dynamics (CFD) simulations for prediction of time–concentration profiles. (A) Schematic depicting confocal microscopy sampling. (B) Concentration–time profiles derived from confocal sampling (corresponding experimental data can be found in Table S6–S9†). (C) Schematic depicting plate reader sampling. (D) Concentration–time profiles derived from plate reader sampling. (E) Spatial molecule mass concentration at four different time points ($t \approx 0$, 0.5, 1.0 and 2.0 h).

computational concentration profiles might be related to the simplifying assumption of pure convective–diffusive transport in the CFD simulation. A saturation during potential interaction of the molecule with the matrix fibers, or molecules secreted by the lymphatic cells such as hyaluronan, could for example easily lead to transport kinetics that cannot be reflected by the concept of apparent diffusion only. As laid out in the discussion later, a model extension that accounts for these potential molecule–matrix interactions might become even more important for the differentiation of antibody transport compared to FITC-dextran molecules. In agreement with previous experimental findings, where a robust fluorescence signal was detected by plate reader sampling between 1 and 2 h for the 150 kDa IgG-DyLight650, the computational assessment of the 150 kDa FITC-dextran molecule shows concentration values between 30% and 80% of the initial concentration in that time frame (Fig. 3D). The variability in predicted concentrations, which is indicated by the error bars in Fig. 3D, results from flow rate variations of one standard deviation observed in the flow rate measurements with fluorescence recovery after photobleaching (FRAP) (Fig. S5†). The time lag for reaching similar concentration levels in the plate reader sampling compared to the local confocal sampling is caused by the mixing of the dextran entering the outlet channel as illustrated in Fig. 3E.

3.3 Impact of antibody aggregation on lymphatic transport on-chip

Upon subcutaneous (SC) administration, monoclonal antibody (mAb) formulations are exposed to the physiological environment of the SC tissue, involving not only changes in pH and temperature but also interactions with various resident cells and extracellular matrix components. This environment can impact the injected mAb, leading to

instability and potential precipitation and/or aggregation at the injection site, resulting in poor lymphatic absorption.[37,38] To test the ability of the lymphatics on-chip model to capture reduced absorption due to mAb aggregation, two well-known physical stressors were used to induce aggregation of IgG-DyLight650 prior to lymphatic transport measurement – shear-stress (stirring) and temperature-stress (heating).[19–21] The migration of IgG through native sodium dodecyl sulfate polyacrylamide (SDS-PAGE) gels was altered for both stressed conditions compared to unstressed control, with some of the protein failing to migrate out of the wells (red circles) (Fig. 4A). Compared to stirred IgG and the unstressed control, the migration of heated IgG showed a smeared pattern in the region of the gel associated with high molecular weight (MW) species, suggesting that this condition led to formation of multimeric IgG species (Fig. 4A). Following both stirring and heating there was significantly less IgG transported across the extracellular matrix (ECM) and into the lymphatic capillaries compared to the unstressed control (Fig. 4B). These results are consistent with our previous observations showing delayed transport of fluorescein isothiocyanate (FITC)-dextrans with increased MW (Fig. 2C) and are also in line with *in vivo* biodistribution experiments showing delayed absorption of IgG1 aggregates from the injection site after SC administration in mice.[39]

3.4 Correlation of *in vitro* lymphatic transport with *in vivo* subcutaneous bioavailability

The *in vitro* lymphatic transport of eight monoclonal antibodies (mAbs) and one fusion protein (FP) with known human subcutaneous (SC) bioavailability was examined to determine if there is a relationship between *in vitro* transport and *in vivo* bioavailability. Of the test set, six of the molecules were arbitrarily considered as having high bioavailability (>60%) and three low bioavailability (<60%) (Fig. 5A).

Based on the previous optimization (Fig. 2D and 3), a 120 min time point was selected to study the percentage lymphatic transport of the full panel of molecules. We observed different percentage transported depending on the molecule, with mAbs with high bioavailability largely showing higher transport on-chip and mAbs with low bioavailability showing lower transport (Fig. 5B). To account for the large variability in the transport data, each molecule was measured in triplicate in four independent experiments. Further, to assess the utility of the on-chip absorption data for ranking SC bioavailability, we performed two analyses: a frequency distribution and a correlation analysis. Visualization of the relative frequencies of mAbs with different % absorption on-chip showed two mAbs above 25% absorption, three mAbs below 15% absorption and four mAbs between 25% and 15% (Fig. S8†). Based on this, we established the 15% and 25% absorption values as cutoff values to bin our data, resulting in three categories as depicted by the dotted lines in Fig. 5B: lines at 25% and 15% denote the thresholds that allow for ranking a mAb as likely to have high (>25%) and low (<15%) bioavailability, respectively. With the currently available data, the range between 15% and 25% is inconclusive and likely to be in the space of high bioavailability. These binning categories are however preliminary and will be refined as we add more molecules to the analysis. Of note, mAb#9, which shows a low SC bioavailability in humans (<20%) due to target-mediated disposition by B cells in the lymphatics, shows a medium-high absorption on-chip (>15%). This discrepancy might be related to the lack of B cells in the lymphatics on-

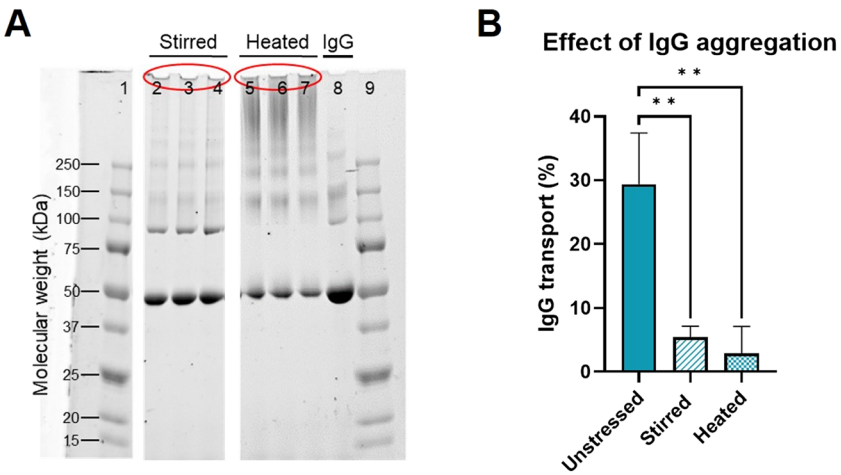

Fig. 4 Impact of antibody aggregation on lymphatic transport on-chip. (A) SDS-PAGE of unstressed (IgG, control), stirred and heated IgG-DyLight650 under native conditions. Lanes 1 and 9: molecular size marker; lanes 2–4: 24 h 300 rpm stirred IgG; lanes 5–7: 12 min 74 °C heat-stressed IgG. (B) Percentage unstressed and stressed IgG-Dylight650 transported across the extracellular matrix (ECM) and lymphatic capillaries after 2 h. Data represent mean ± SD (n = 3). A one-way ANOVA with Tukey's multiple comparisons test was performed to compare IgG percentage transport (**$P \leq 0.01$).

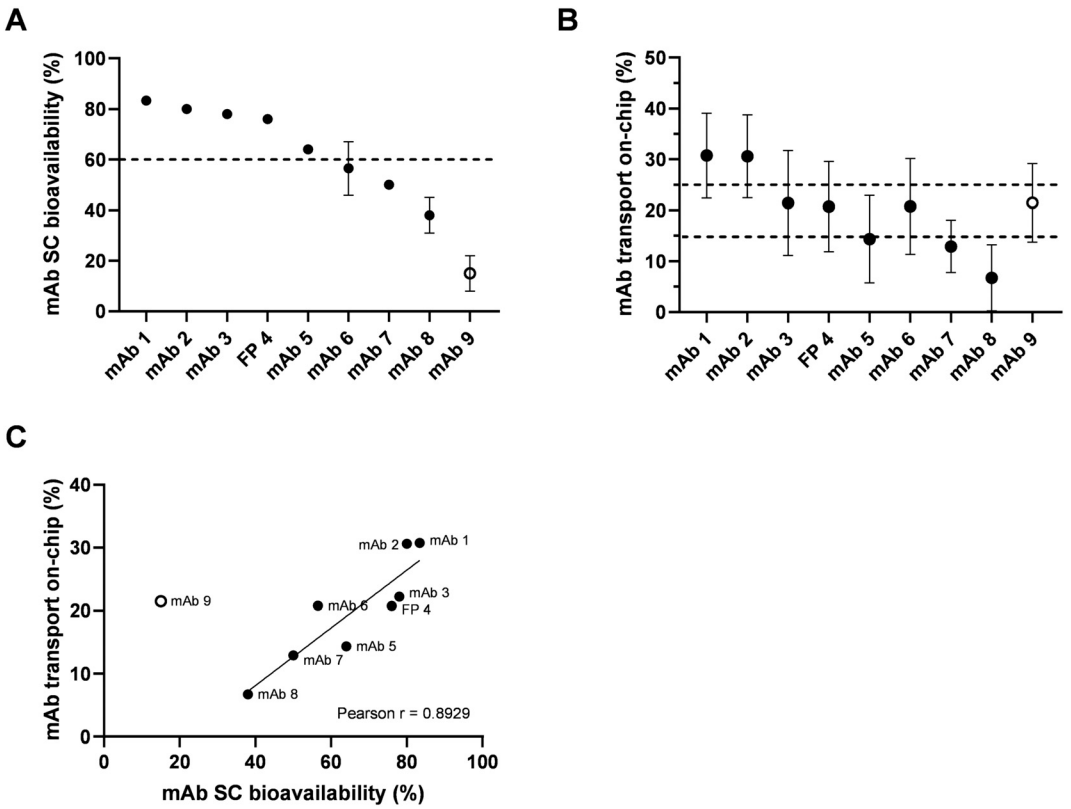

Fig. 5 Lymphatic transport on-chip of a panel of protein molecules and *in vitro–in vivo* correlation (IVIVC) with subcutaneous bioavailability in humans. (A) Subcutaneous (SC) bioavailability in humans of the panel of 9 molecules selected for the study. For the purpose of this study, SC bioavailability >60% is considered high and below 60% is considered low. mAb#9 is depicted with an empty circle because it is subject to target-mediated disposition by B cells in the lymphatics. SC bioavailability for mAb 7 is an estimate from a population PK model used in the absence of clinical IV PK data. (B) Percentage protein transported on-chip at 120 min time point for the panel of 9 molecules. Dotted lines at 25% and 15% denote proposed thresholds for ranking a molecule as likely to have high and low bioavailability, respectively. The space between 15% and 25% is inconclusive and likely to be in the high bioavailability range (>60%). Data represent mean ± SD of four independent experiments measuring each molecule in triplicate. (C) IVIVC of percentage lymphatic absorption on-chip and SC bioavailability showing a linear regression and Pearson analysis excluding mAb#9.

chip system compared to *in vivo*, where they contribute to the low plasma exposure of mAb#9. A correlation analysis performed without the outlier mAb#9, showed a good linear relationship between the % absorption on-chip and the SC bioavailability in humans (Fig. 5C). Pearson analysis also showed a strong correlation (r = 0.8929), highlighting the potential of the lymphatics on-chip model to rank order SC absorption of mAb candidates in development.

4. Discussion

A limitation in our understanding of the systemic absorption of therapeutic proteins following their subcutaneous (SC) administration is a lack of predictive preclinical models for translation to humans.[40] Because of their size and poor passive permeability, large molecular weight biotherapeutics (>16 kDa), such as monoclonal antibodies (mAbs), are largely excluded from entering the blood circulation following SC administration, but instead are absorbed into the 'leakier' lymphatic vasculature for delivery *via* the thoracic duct to the blood circulation.[41] Aiming to recapitulate SC lymphatic transport *in vitro*, Serrano *et al.*[14] developed a microphysiological system (MPS) where lymphatic network sprouting and proliferation were responsive to applied growth factors and interstitial flow velocities. This system allowed for measurement of drainage rate (*i.e.*, lymphatic absorption) from the interstitial space into the lymphatic capillaries of a variety of macromolecules, including dextrans, albumin and antibodies.[14,24] Building on this on-chip lymphatic system, the main goals of this work were to (1) streamline the workflow by increasing speed and throughput and (2) establish an *in vitro–in vivo* correlation (IVIVC) for nine proteins for which bioavailability in humans following SC administration is known.

As we slightly modified the methods outlined in Serrano *et al.*[14] to induce lymphatic sprouting over a shorter culture period, an initial step was to validate the system for suitability in IVIVC based on its ability to recapitulate the morphology, phenotypic marker expression and drainage rates of subdermal lymphatics *in vivo*. Application of interstitial flow velocity in the physiological range (~1 μm s^{-1})[26] to the inlet channel of the chips during culturing, in

combination with growth factors, led to the development of extensive lymphatic networks extending into the interstitial space. Together with interstitial flow and growth factor signaling, previous studies have highlighted the impact of matrix mechanical properties on lymphatic vessel development. In particular, soft substrates in the range of 0.2 kPa have been shown to enhance lymphatic capillary formation,[27–29] partially by promoting an increased vascular endothelial growth factor receptor 3 and matrix metalloproteinase expression.[29] The modulation of fibrinogen and thrombin concentrations has been extensively studied to tune fibrin matrix stiffness and porosity, and a stiffness below 0.2 kPa, within the optimal range for lymphatic vessel formation, has been reported for fibrin ECMs with similar compositions to the present study.[42–44] Supporting the evidence that soft substrates favor LEC sprouting, our results showed an impaired lymphatic capillary formation in fibrin matrices of 5 *vs.* 2.5 mg mL^{-1}, likely attributed to both an increased stiffness and decreased porosity in the ECMs with higher fibrinogen concentration.[35,36,43]

The lymphatic endothelial cell networks on-chip expressed lymphatic vessel endothelial receptor 1 (LYVE-1) and vascular endothelial-cadherin (VE-cadherin), both canonical markers of lymphatic capillary endothelium,[45,46] and capillary lumens could be identified close to the lymphatic tubule (Fig. S11†). In addition, their density and length were in line with morphological features of healthy subdermal lymphatics *in vivo*[30–32] as well as with previously described lymphatics on-chip models.[14] To further confirm that the lymphatics on-chip presented a lymphatic capillary rather than a collecting-vessel phenotype, we analyzed the expression of FOXC2, a transcription factor expressed in lymphatic collecting vessels in response to flow.[33,34] Our results revealed a reduced expression of FOXC2 mRNA in LECs on-chip compared to LECs cultured on tissue culture flasks, supporting the induction of a lymphatic capillary phenotype in the lymphatics on-chip model (Fig. S10†). Although the density of lymphatic vessels can vary in diseased states, it was not the purpose of the present study to evaluate the influence of such changes on SC lymphatic absorption. The natural biological variability observed in capillary growth from chip to chip was accounted for by including at least three biological replicates per molecule measured, and by repeating the experimental measurement on at least three different days, in order to minimize any potential impact on drainage rate. Importantly, testing of lymphatic transport of a validation set of molecules (FITC-dextrans of 4, 150 and 500 kDa and IgG) in the optimized lymphatics on-chip resulted in drainage rate values in range with values measured in mouse, rat and rabbit preclinical animal models (~0.02–0.005 min^{-1})[47–52] as observed by Serrano *et al.*[14] In agreement with previous work by Serrano *et al.*, size-dependent discrimination was observed when calculating drainage rate from concentration profiles early in the assay (*i.e.*, 10 min), whereas resolution was lost at later time points (Fig. 2C), highlighting the importance of time point selection for rank ordering lymphatic transport.

Expanding on the imaging-based methodologies used to analyze lymphatic transport on-chip, here we developed a plate reader-based fluorescence spectroscopy approach. This methodology was preferred for the testing of our internal mAb set given the amenability for application of analytical procedures other than fluorescence spectroscopy (*e.g.*, ligand binding assays, LC–MS/MS) as well as ease of use and the potential for increased throughput. In agreement with the size-dependent molecule discrimination previously observed by confocal measurements, reducing the porosity of the extracellular matrix by increasing fibrinogen content or eliciting antibody aggregation prior to administration to the inlet channel led to reductions in the amount of IgG transported into the lymphatics. Consistent with our results, previous work has demonstrated the dependency of molecule transport on matrix composition[11] and pointed to the impact of antibody aggregation at the injection site on SC bioavailability *in vivo*.[39,53] The data generated with our on-chip lymphatic system suggest that both molecule/matrix and molecule/molecule interactions can influence SC absorption and support the hypothesis that mAb aggregation may be one of the key contributors to low SC bioavailability.

Compared to the concentration–time profiles observed during confocal sampling, which started to reach plateau values at around 30 min, the plate reader sampling resulted in an apparent delay in lymphatic transport, with maximum values taking longer to achieve. The observed temporal differences between the two analytical methods are likely attributed to the direct (confocal) *vs.* indirect (plate-reader) sampling methods, and for the latter, dilution of the sample prior to analysis leading to an apparent delayed signal appearance. Indeed, computational fluid dynamics (CFD)-based simulations showed that dilution of the samples prior to fluorescence detection by plate reader-based spectroscopy could account for the temporal differences observed experimentally. Interestingly, the CFD based convection–diffusion simulations were unable to differentiate between absorption of FITC-dextrans of varying molecular weight based on the differences between their diffusion coefficient alone (Fig. 3C), implying that additional factors contribute to molecule transport in the on-chip system. Inclusion of reversible and irreversible molecule–molecule and molecule–matrix interactions into the CFD simulations along with testing these hypotheses using experimental models such as the lymphatics on-chip system should help improve predictions of lymphatic absorption following SC delivery. Also for future consideration are the sink conditions which were used in the on-chip system, as this does not account for molecule diffusion from the lymphatic capillary into the extracellular matrix nor transport kinetics within the lymphatic vessel. More detailed models like the single lymph vessels model presented by Serrano *et al.*[14] perhaps better represent these mechanisms but are limited in the spatial

dimension of the modelled domain and therefore are not easily adjustable for the simulations of complete MPS. Our convenient scalable approach is therefore well-suited for integration into macroscopic physiological applications like SC injection simulations or delivery to local targets in the tissue[25] but comes with the above-mentioned limitations. Nevertheless, we are confident that by better recapitulating physiological tissue conditions on-chip (*e.g.* use of collagen, hyaluronan, and proteoglycan fibers instead of fibrin as ECM components; inclusion of additional cell types representative of the subdermal microenvironment), especially for the absorption of mAbs, the molecule transport and retention will become more dominated by local charge related molecule–matrix interactions, emphasizing the importance to extend the computational and experimental modeling capacities into this area next.

Establishing *in vitro–in vivo* correlation aids in evaluating the predictive power of *in vitro* models including the lymphatics on-chip system, and prediction of SC bioavailability may help limit the number of *in vivo* animal studies needed for therapeutic protein development.[54] It was not the intent of the present study to necessarily develop IVIVC for absolute SC bioavailability prediction, but instead for rank ordering mAbs based on their lymphatic absorption, setting the stage for selection of most promising preclinical candidates to move toward the clinic. All nine proteins tested had SC bioavailability data available from human clinical studies, with bioavailability ranging from ~15% to ~80%. The extent of lymphatic absorption *in vitro* and human bioavailability *in vivo* showed a positive linear relationship for eight of the nine proteins tested. The outlier was a mAb that is known to undergo target-mediated lymphatic clearance by B cells, leading to its apparent low bioavailability *in vivo* (~15%). The lymphatics on-chip model does not include circulating B cells, which could explain why, based on our observed transport data, this mAb would be characterized as having moderate SC bioavailability. Further experiments on-chip conducted in the presence of B cells would be needed to validate this hypothesis. The SC bioavailability values for all other proteins used for IVIVC were ~40–80%, consistent with values generally observed for marketed therapeutic mAbs (50–80%).[55] We acknowledge that this is not a large range of values, and, considering the experiment variability in transport measurements, identifying compounds at the extreme ends of the range may be the most useful feature of the on-chip assay as it applies to screening of mAbs for their SC bioavailability potential. Monoclonal antibodies showing transport levels on-chip of >25% and <15% are predicted to have SC bioavailability values at either end of the clinically observed range. We speculate that a potential source of variability in the transport measurements is related to the poor flow control provided by the current model. On the one hand, a poor control over the syringe-based high flow used during the lymphatic growth phase can result in variability in lymphatic ECM coverage. On the other hand, variability in the luer-based low flow used for the lymphatic transport measurements can directly impact the resulting convective transport rates. This is in agreement with CFD simulations showing a large impact of luer-flow variability on the transport of FITC-dextrans of 4 and 150 kDa (Fig. 3D). Next developments of this model should include refinements in flow control to improve its robustness and fidelity. Another limitation of the present model is that it assumes that diffusion and convection through the extracellular matrix (ECM) and absorption into the lymphatics are the rate-limiting steps. However, a variety of other factors related to sub-dermal physiology could limit the ability of mAbs to reach the systemic circulation,[40] such as metabolic instability at the injection site,[54] local non-specific uptake by resident cells, or in the case of mAb#9 in the present study, target-mediated disposition.

Drug product-related factors can also influence absorption from the SC injection site into the lymphatics, including physicochemical properties of the molecule, formulation/excipients (especially excipients that may enhance absorption such as hyaluronidase[56]), device injection rates, volume of injection and dose. Previously described *in vitro* models have specifically explored the impact of mAb physicochemical properties and formulations on SC absorption and found a good correlation with SC bioavailability data.[57–59] Recently, a subdermal MPS model examined the physicochemical properties of mAbs and their impact on subdermal endothelial permeability/drainage and ECM binding.[24] Although the individual mAbs examined in this work were applied to the on-chip assay after dilution in cell culture medium rather than in their original formulation, they exhibited different degrees of interaction with the ECM that correlated with the mAb propensity for aggregation. Taken together, this evidence indicates that the events leading to reduction in SC bioavailability of protein drugs are predominantly occurring in the SC space, a hypothesis further supported by a recently described *in vivo* and *in silico* approach for predicting the SC bioavailability of antibody drugs.[60] In addition to the usefulness of the lymphatics on-chip model in selecting mAb candidates with the greatest potential for SC absorption, it should prove useful for better understanding the underlying mechanisms and for identifying input parameters for more refined computational analysis in the future.

5. Conclusions

In vitro tools to predict the systemic exposure of monoclonal antibodies (mAbs) following their subcutaneous (SC) administration are lacking. With the goal of filling this translational knowledge gap we established an on-chip lymphatic system recapitulating the subdermal lymphatic capillary network *in vivo*. The transport rate of macromolecules through the extracellular matrix into the lymphatic capillary bed differed for the molecules tested. Factors influencing lymphatic transport

on-chip included molecular size, extracellular matrix composition, and aggregation. An *in vitro–in vivo* correlation (IVIVC) for eight mAbs and one fusion protein in the market and in clinical development suggested a positive correlation between lymphatic transport on-chip and their SC bioavailability in humans. The data highlight the potential use of the lymphatics on-chip model to classify *a priori* therapeutic mAbs as having high, moderate, or low SC bioavailability potential. Furthermore, it supports the hypothesis that the loss in SC bioavailability for most mAbs is mainly occurring in the SC space. Future work should focus on developing engineering solutions for more robust flow control and in developing on-chip and computational models for quantitatively predicting the SC bioavailability of mAbs as well as other therapeutic modalities transported *via* the lymphatic system. Combined with computational efforts, the lymphatics on-chip model offers the opportunity to investigate the drug properties and physiological factors that influence lymphatic absorption and can be useful to inform molecule and formulation design for optimal SC absorption.

Data availability

Data for this article, including fluorescein isothiocyanate (FITC)-dextran concentration–time profiles and drainage rates, FITC-dextran diffusion coefficients, parameters used in the simulations (*e.g.* microfluidic chip geometry details; fluid, gel and membrane properties) and frequency distribution analysis of monoclonal antibody and fusion protein transport on-chip can be found in the ESI† and are cited throughout the text.

Some information regarding the panel of antibodies and fusion protein tested in this work, including molecule name, sequence or their absolute subcutaneous human bioavailability values used for the *in vitro–in vivo* correlations, cannot be made available due to legal confidentiality requirements.

Author contributions

Adriana Martinez Ledo: conceptualization, methodology, investigation, writing – original draft, writing – review & editing. Gabriela Misiewicz: methodology, investigation, writing – original draft, writing – review & editing. Thomas Dimke: conceptualization, methodology, investigation, writing – original draft, writing – review & editing. William R. Tschantz: methodology, investigation, writing – original draft, writing – review & editing. Jillian Handel: methodology, investigation, writing – review & editing. Ryan Pelis: conceptualization, writing – original draft, writing – review & editing. Gerard Bruin: conceptualization, writing – original draft, writing – review & editing. Karoline Bechtold-Peters: conceptualization, writing – review & editing, funding acquisition. Manuel Sanchez-Felix: conceptualization, writing – review & editing. Sujal Deshmukh: writing – review & editing, funding acquisition, supervision. Seunggyu Kim: conceptualization, methodology, writing – review & editing. Maria Proestaki: conceptualization, methodology, writing – review & editing. Roger Kamm: conceptualization, methodology, writing – review & editing.

Conflicts of interest

A. M. L., G. M., T. D., W. R. T., R. P., G. B., K. B. P. and S. D. declare to work at Novartis AG. A. M. L., G. M., T. D., W. R. T., R. P., G. B., K. B. P., M. S.-F. and S. D. declare to hold stock in Novartis AG. R. D. K. is the co-founder of and holds a significant financial interest in AIM Biotech, a company that produces microfluidic devices. He also receives research support from Amgen, Daiichi-Sankyo, Novartis, Boehringer Ingelheim, AbbVie, Takeda, Eisai, Visterra, EMD Serono and Roche. The authors declare no other potential conflicts of interest with respect to the research, authorship, and/or publication of this article.

Acknowledgements

The authors acknowledge Georgios Pavlou and Dallas Bednarczyk for scientific discussion and support. The authors thank Ishan Gupta, Ned Kirkpatrick, Jon Horvath and Tessa Morris for their help with confocal imaging and MATLAB analysis. The authors are grateful to Christopher Schwalen for sharing his expertise on SDS-PAGE.

References

1 J. Bolleddula, K. Brady, G. Bruin, A. Lee, J. A. Martin, M. Walles, K. Xu, T. Y. Yang, X. Zhu and H. Yu, *Drug Metab. Dispos.*, 2022, **50**, 837–845.
2 B. Bittner, W. Richter and J. Schmidt, *BioDrugs*, 2018, **32**, 425–440.
3 C. A. Walsh, P. Minnock, C. Slattery, N. Kennedy, F. Pang, D. J. Veale, B. Bresnihan and O. FitzGerald, *Rheumatology*, 2007, **46**, 1148–1152.
4 E. Hedayati, L. Fracheboud, V. Srikant, D. Greber, S. Wallberg and C. L. Stragliotto, *PLoS One*, 2019, **14**, e0211783.
5 E. De Cock, X. Pivot, N. Hauser, S. Verma, P. Kritikou, D. Millar and A. Knoop, *Cancer Med.*, 2016, **5**, 389–397.
6 X. Pivot, J. Gligorov, V. Muller, G. Curigliano, A. Knoop, S. Verma, V. Jenkins, N. Scotto, S. Osborne, L. Fallowfield and G. PrefHer Study, *Ann. Oncol.*, 2014, **25**, 1979–1987.
7 F. Zheng, P. Hou, C. D. Corpstein, K. Park and T. Li, *J. Controlled Release*, 2021, **337**, 407–416.
8 G. J. Randolph, S. Ivanov, B. H. Zinselmeyer and J. P. Scallan, *Annu. Rev. Immunol.*, 2017, **35**, 31–52.
9 K. L. Gill, I. Gardner, L. Li and M. Jamei, *AAPS J.*, 2016, **18**, 156–170.
10 S. A. Stacker, S. P. Williams, T. Karnezis, R. Shayan, S. B. Fox and M. G. Achen, *Nat. Rev. Cancer*, 2014, **14**, 159–172.

11 W. F. Richter, S. G. Bhansali and M. E. Morris, *AAPS J.*, 2012, **14**, 559–570.
12 S. G. Uzel, O. C. Amadi, T. M. Pearl, R. T. Lee, P. T. So and R. D. Kamm, *Small*, 2016, **12**, 612–622.
13 S. Kim, M. Chung and N. L. Jeon, *Biomaterials*, 2016, **78**, 115–128.
14 J. C. Serrano, M. R. Gillrie, R. Li, S. H. Ishamuddin, E. Moeendarbary and R. D. Kamm, *Adv. Sci.*, 2024, **11**, e2302903.
15 N. Frenkel, S. Poghosyan, C. R. Alarcón, S. B. García, K. Queiroz, L. van den Bent, J. Laoukili, I. B. Rinkes, P. Vulto, O. Kranenburg and J. Hagendoorn, *ACS Biomater. Sci. Eng.*, 2021, **7**, 3030–3042.
16 J. Schindelin, I. Arganda-Carreras, E. Frise, V. Kaynig, M. Longair, T. Pietzsch, S. Preibisch, C. Rueden, S. Saalfeld, B. Schmid, J. Y. Tinevez, D. J. White, V. Hartenstein, K. Eliceiri, P. Tomancak and A. Cardona, *Nat. Methods*, 2012, **9**, 676–682.
17 M. H. Elfarnawany, *Doctor of Philosophy*, The University of Western Ontario, 2015.
18 P. Jönsson, M. P. Jonsson, J. O. Tegenfeldt and F. Höök, *Biophys. J.*, 2008, **95**, 5334–5348.
19 A. Hawe, J. C. Kasper, W. Friess and W. Jiskoot, *Eur. J. Pharm. Sci.*, 2009, **38**, 79–87.
20 V. Filipe, R. Poole, O. Oladunjoye, K. Braeckmans and W. Jiskoot, *Pharm. Res.-Dordr.*, 2012, **29**, 2202–2212.
21 M. K. Joubert, Q. Luo, Y. Nashed-Samuel, J. Wypych and L. O. Narhi, *J. Biol. Chem.*, 2011, **286**, 25118–25133.
22 Siemens, *Siemens Digital Industries Software*, Simcester STAR-CCM+ User Guide, version 2021.1, 2021.
23 J. B. Freund, J. G. Goetz, K. L. Hill and J. Vermot, *Development*, 2012, **139**, 3063.
24 G. S. Offeddu, J. C. Serrano, Z. Wan, M. A. Bryniarski, S. C. Humphreys, S. W. Chen, H. Dhoolypala, K. Conner and R. D. Kamm, *ALTEX*, 2023, **40**, 299–313.
25 M. Soltani and P. Chen, *J. Biol. Eng.*, 2012, **6**(1), 4.
26 S. R. Chary and R. K. Jain, *Proc. Natl. Acad. Sci. U. S. A.*, 1989, **86**, 5385–5389.
27 L. Alderfer, E. Russo, A. Archilla, B. Coe and D. Hanjaya-Putra, *FASEB J.*, 2021, **35**(5), e21498.
28 L. Alderfer, S. Saha, F. Fan, J. M. Wu, L. E. Littlepage and D. Hanjaya-Putra, *Commun. Biol.*, 2024, **7**, 1262.
29 M. Frye, A. Taddei, C. Dierkes, I. Martinez-Corral, M. Fielden, H. Ortsäter, J. Kazenwadel, D. P. Calado, P. Ostergaard, M. Salminen, L. Q. He, N. L. Harvey, F. Kiefer and T. Mäkinen, *Nat. Commun.*, 2018, **9**, 1511.
30 Y. Zhang, M. H. Ulvmar, L. Stanczuk, I. Martinez-Corral, M. Frye, K. Alitalo and T. Makinen, *Nat. Commun.*, 2018, **9**, 1296.
31 S. Lutter, S. Xie, F. Tatin and T. Makinen, *J. Cell Biol.*, 2012, **197**, 837–849.
32 A. Milasan, F. Dallaire, G. Mayer and C. Martel, *Sci. Rep.*, 2016, **6**, 27862.
33 M. N. Hernández Vásquez, M. H. Ulvmar, A. González-Loyola, I. Kritikos, Y. Sun, L. He, C. Halin, T. V. Petrova and T. Mäkinen, *EMBO J.*, 2021, **40**(12), e107192.
34 W. L. Murfee, J. W. Rappleye and G. W. Schmid-Schönbein, *FASEB J.*, 2007, **21**, A490.
35 I. K. Piechocka, R. G. Bacabac, M. Potters, F. C. MacKintosh and G. H. Koenderink, *Biophys. J.*, 2010, **98**, 2281–2289.
36 K. A. Leonidakis, P. Bhattacharya, J. Patterson, B. E. Vos, G. H. Koenderink, J. Vermant, D. Lambrechts, M. Roeffaers and H. Van Oosterwyck, *Acta Biomater.*, 2017, **47**, 25–39.
37 M. Viola, J. Sequeira, R. Seiça, F. Veiga, J. Serra, A. C. Santos and A. J. Ribeiro, *J. Controlled Release*, 2018, **286**, 301–314.
38 H. M. Kinnunen and R. J. Mrsny, *J. Controlled Release*, 2014, **182**, 22–32.
39 V. Filipe, I. Que, J. F. Carpenter, C. Lowik and W. Jiskoot, *Pharm. Res.*, 2014, **31**, 216–227.
40 M. Sánchez-Félix, M. Burke, H. H. Chen, C. Patterson and S. Mittal, *Adv. Drug Delivery Rev.*, 2020, **167**, 66–77.
41 A. Supersaxo, W. R. Hein and H. Steffen, *Pharm. Res.*, 1990, **7**, 167–169.
42 K. A. Jansen, R. G. Bacabac, I. K. Piechocka and G. H. Koenderink, *Biophys. J.*, 2013, **105**, 2240–2251.
43 H. Duong, B. Wu and B. Tawil, *Tissue Eng., Part A*, 2009, **15**, 1865–1876.
44 J. Liu, Y. H. Tan, H. F. Zhang, Y. Zhang, P. W. Xu, J. W. Chen, Y. C. Poh, K. Tang, N. Wang and B. Huang, *Nat. Mater.*, 2012, **11**, 734–741.
45 D. G. Jackson, *APMIS*, 2004, **112**, 526–538.
46 D. Vestweber, *Arterioscler., Thromb., Vasc. Biol.*, 2008, **28**, 223–232.
47 S. Karaman, D. Buschle, P. Luciani, J. C. Leroux, M. Detmar and S. T. Proulx, *Angiogenesis*, 2015, **18**, 489–498.
48 P. Zbyszynski, I. Toraason, L. Repp and G. S. Kwon, *Nano Convergence*, 2019, **6**, 22.
49 A. K. Polomska, S. T. Proulx, D. Brambilla, D. Fehr, M. Bonmarin, S. Brändli, M. Meboldt, C. Steuer, T. Vasileva, N. Reinke, J. C. Leroux and M. Detmar, *JCI Insight*, 2019, **4**(4), e126515.
50 T. N. Doan, F. C. Bernard, J. M. McKinney, J. B. Dixon and N. J. Willett, *Acta Biomater.*, 2019, **93**, 270–281.
51 D. Brambilla, S. T. Proulx, P. Marschalkova, M. Detmar and J. C. Leroux, *Small*, 2016, **12**, 1053–1061.
52 E. Guc, P. S. Briquez, D. Foretay, M. A. Fankhauser, J. A. Hubbell, W. W. Kilarski and M. A. Swartz, *Biomaterials*, 2017, **131**, 160–175.
53 M. R. Turner and S. V. Balu-Iyer, *J. Pharm. Sci.*, 2018, **107**, 1247–1260.
54 D. Li, P. Y. Chow, T. P. Lin, C. Cheow, Z. Li and M. G. Wacker, *J. Pharm. Sci.*, 2023, **112**, 1492–1508.
55 N. L. Dirks and B. Meibohm, *Clin. Pharmacokinet.*, 2010, **49**, 633–659.
56 R. L. Murray and A. Z. Gondal, in *StatPearls*, Treasure Island (FL) ineligible companies. Disclosure: Anoosh Zafar Gondal declares no relevant financial relationships with ineligible companies, 2024.
57 H. Lou, C. Berkland and M. J. Hageman, *Int. J. Pharm.*, 2021, **605**, 120824.

58 H. K. Bown, C. Bonn, S. Yohe, D. B. Yadav, T. W. Patapoff, A. Daugherty and R. J. Mrsny, *J. Controlled Release*, 2018, **273**, 13–20.
59 H. M. Kinnunen, V. Sharma, L. R. Contreras-Rojas, Y. Yu, C. Alleman, A. Sreedhara, S. Fischer, L. Khawli, S. T. Yohe, D. Bumbaca, T. W. Patapoff, A. L. Daugherty and R. J. Mrsny, *J. Controlled Release*, 2015, **214**, 94–102.
60 T. Birngruber, Joanneum Research, A novel in vivo/in silico approach for predicting bioavailability of subcutaneously administered antibody drugs, *Oral presentation at CRS Annual Meeting 2024*, Bologna, Italy, 2024.